CCFE
CULHAM CENTRE FOR FUSION ENERGY

UK Atomic Energy Authority

UKAEA-CCFE-PR(20)86

Alexander J. Leide, Richard. Todd, David E. J. Armstrong

Indentation residual stress and evolution of fracture during FIB cross-sectioning

Enquiries about copyright and reproduction should in the first instance be addressed to the UKAEA Publications Officer, Culham Science Centre, Building K1/0/83 Abingdon, Oxfordshire, OX14 3DB, UK. The United Kingdom Atomic Energy Authority is the copyright holder.

The contents of this document and all other UKAEA Preprints, Reports and Conference Papers are available to view online free at scientific-publications.ukaea.uk/

Indentation residual stress and evolution of fracture during FIB cross-sectioning

Alexander J. Leide, Richard. Todd, David E. J. Armstrong

This is a preprint of a paper submitted for publication in
To be decided

Indentation residual stress and evolution of fracture during FIB cross-sectioning

Alexander J. Leide[1*], Richard I. Todd[1], and David E. J. Armstrong[1]

[1] *Department of Materials, University of Oxford*
Parks Road, Oxford, OX1 3PH, UK

email*:* *alexander.leide@materials.ox.ac.uk*

Abstract. Focussed ion beam (FIB) milling can be used to reveal sub-surface fracture and deformation below indents in materials. However, evolution of residual stresses around the indent impression cause changes to the crack morphology during the FIB cross-sectioning procedure. Berkovich nanoindents in single crystal hexagonal (6H) silicon carbide cause radial surface cracks, and the residual stresses are mapped using Raman piezospectroscopy and high angular resolution EBSD. FIB milling changes the stress state, allowing surface cracks to extend, and sub-surface cracks to evolve, precluding direct observation of sub-surface crack morphology using this technique. Raman spectroscopy after FIB milling reveals that the compressive residual stress has been relieved allowing crack extension. Ion irradiation damage subdues cracking in 6H-SiC, and differences in residual stress maps explain the role of cracking in relieving residual tensile hoop stress around indents.

Keywords: nanoindentation; residual stress; FIB milling; fracture; ion irradiation

Introduction

Fracture toughness is an important property to measure in brittle materials to help design against sudden catastrophic failure. This can be estimated using indentation techniques combined with semi-empirical equations by measuring surface crack lengths and indentation load. The empirical equation is based on the indenter geometry and assumed sub-surface crack morphology [1–3].

For certain applications it is desirable to evaluate the properties of very small volumes of material, for example to study the effects of radiation damage in ion irradiated materials [4,5]. This is typically done using nanoindentation with a Berkovich tip geometry to measure radiation-induced changes to hardness and modulus, and it would be desirable to also measure changes to fracture toughness.

Fracture toughness from Berkovich geometry indents has been estimated using the modified Laugier equation [6] from Dukino and Swain [7,8]:

$$K_c = x_v \left(\frac{a}{l}\right)^{1/2} \left(\frac{E}{H}\right)^{2/3} \frac{P}{c^{3/2}} \quad (1)$$

where K_c is the fracture toughness, a is indent impression radius from the centre of the impression to the corner, l is surface crack length, E is Young's modulus, H is hardness, P is maximum indenter load, and c, is the length from the centre of the indent impression to the crack tip, ie $a+l$. x_v is a fitting factor with a value 0.016. This equation is valid for the Palmqvist radial crack system with the fitting factor for Berkovich geometry derived from fitting to fracture toughness from conventional micro-Vickers indents [7].

Cuadrado *et al.* used single edge-notch beam fracture toughness measurements to fit the Laugier equation for Berkovich nanoindentation fracture toughness, finding a fitting factor of $x_v = 0.022$ [9]. They also used FIB tomography to observe sub-surface fracture finding semi-elliptical radial cracks, meeting at the apex of the indent impression. This 38% difference in x_v will propagate into a 38% difference in estimated fracture toughness from Berkovich nanoindentation. This discrepancy highlights the drawbacks of measuring fracture toughness using indentation techniques – the result is dependent on empirical constants and assumptions, some of which require knowledge of sub-surface fracture to validate.

Dual beam focussed ion beam scanning electron microscopes (FIB/SEM) allow nanoscale milling to reveal sub-surface features of materials for imaging with the SEM column [10,11]. This technique has been used to investigate sub-surface indentation fracture in alumina [12], silicate glass [13], SiAlON [14], and silicon nitride [15]. Local residual stresses were observed to cause bulging of FIB cross-sections, and the direction of FIB milling through the indent changed the observed crack density as residual stresses were relieved [12,13].

Silicon carbide (SiC) is a structural ceramic material useful in extreme environments, primarily aerospace and nuclear applications, because of its excellent high-temperature properties, including creep resistance, high strength at elevated temperatures, corrosion resistance and general chemical inertness, high thermal conductivity, and low thermal expansion coefficient [16–18]. SiC is desirable for applications as fission fuel cladding, or as a component of the blanket of fusion reactors due to its low neutron absorption cross-section, low level of long-lived radioisotopes, and stability under high temperature-high dose neutron irradiation [16,19–24].

For nuclear applications, a thorough understanding of radiation defects and their effects on material properties including fracture toughness is required to evaluate the suitability of a material for its application, and to predict the evolution of its properties over time. To accelerate radiation damage processes and material investigations, ion implantation is commonly used as a surrogate for neutron irradiation [25,26]. It allows displacement damage to be introduced to a material in controlled conditions in a matter of hours as compared to many days for comparable damage in a nuclear fission reactor. Additionally, it does not introduce radiological hazards due to sample activation, avoiding the requirements for specialist "active" laboratories, sample cooling, and remote handling.

Jiang *et al.* reported on indentation fracture toughness after xenon ion implantation into 4H-SiC at room temperature, finding fracture toughness apparently increases with dose and in proportion to out of plane elastic strain caused by radiation swelling, up to ~75% apparent toughening [27]. They attribute the crack shortening to lateral compressive strain in the irradiated layer. Nogami *et al.* report on indentation fracture toughness of nanocrystalline 3C CVD SiC after neutron irradiation, finding a decrease of ~10% below 400 °C and an increase above ~800 °C, although with large scatter, possibly due to microstructure effects [28]. Jiang *et al.* [27] do not give their equation for fracture toughness calculations, while Nogami *et al.*

[28] use a mix of values from Vickers and Berkovich indentation which puts their calculations in doubt.

We aim to investigate the residual stresses around nanoindents in unirradiated and irradiated silicon carbide, exploring how fracture influences residual stress. Sub-surface fracture is investigated using FIB cross-sectioning, and the effect of this on residual stress around indents.

Methods

A pre-polished sample of 6H-SiC single crystal, with surfaces parallel to the (0001) basal plane was purchased from Pi-Kem Ltd (Tamworth, UK). Ion implantation was carried out at the Surrey Ion Beam Centre, UK using the 2 MV Van de Graaf accelerator. Samples were clamped to a heated stage using washers to blank part of the specimen from the ion beam, leaving an unirradiated region for investigation. The stage was held at 300 °C (±5 °C) in a vacuum of ~1×10^{-6} mbar. The sample was implanted with neon ions at three energies (1450 keV, 720 keV, and 350 keV) to create a flattened damage profile within the plastic zone of nanoindentations (Figure 1). Neon ions were chosen to avoid any chemical effects from the implanted ions, while producing a similar damage profile to our other work using silicon ions. Self-ions are typically chosen for metals to avoid chemical effects; however literature and our own work suggests implanting SiC with silicon or carbon ions affects defect types compared to neutron irradiations [29]. Chemical defects are important in SiC, so influencing defect chemistry with ion implantation should be avoided [30]. Displacements per atom (dpa) was calculated using the Stopping and Range of Ions in Matter (SRIM) Monte Carlo code with the quick Kinchin-Pease model [31,32]. Displacement energies for silicon and carbon were 35 eV and 21 eV respectively, with binding energies set to 0 eV [33]. Target density was set to 3.21 g/cm^3. The peak nominal damage is ~2.5 dpa.

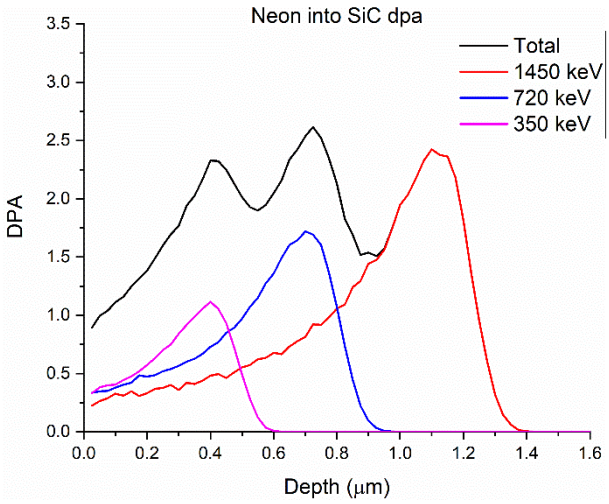

Figure 1: Damage profile of neon ion implantation into 6H-SiC, as calculated from SRIM [31]

Nanoindentation was carried out using an MTS Nanoindenter XP with a diamond Berkovich tip. The continuous stiffness method (CSM) was used to calculate mechanical properties. The CSM harmonic displacement was 2 nm with a frequency of 45 Hz and a strain rate of 0.05 s^{-1}. The tip and frame were calibrated based on the modulus of fused silica (72 GPa) before each batch of indents in a sample. Nanoindentation consisted of batches of 500 nm and 1000 nm indents into irradiated and blanked (unirradiated) regions of the same sample at the same crystallographic orientation. This was to ensure the indentations were carried out with the same tip calibration and condition, sample mounting, and environmental conditions for comparing the effects of ion implantation and to avoid systematic errors. Orientation with respect to the Berkovich tip of the sample was kept constant for unirradiated and irradiated indentation. Details of changes to hardness and elastic modulus are presented in more detail in **[reference nanoindentation stress paper].**

To investigate sub-surface fracture, indents were cross-sectioned using a Zeiss Auriga dual beam FIB-SEM. An initial coarse trench was milled away from the indent at 30 kV 4 nA Ga+ ions to reveal a sub-surface cross-section to the SEM field of view, then fine slices ~30 nm thick were milled at 30 kV 240 pA with automated image acquisition after every three slices.

EBSD experiments were conducted using a Zeiss Merlin FEG-SEM with a Bruker Quantax e-flash detector controlled using Bruker Esprit 2.1 software. Typical SEM conditions were 20 kV 20 nA with an acquisition time of 50 ms per pixel, although these were varied depending on experimental time constraints and pattern quality. Patterns were acquired with 800x600 pixel resolution and were all saved so that they could be analysed offline using the

high angular resolution EBSD code, XEBSD developed at the Department of Materials, University of Oxford, and Imperial College, London [34–36].

The procedure for analysing EBSD patterns using high angular resolution is explained fully in refs. [37,38], but will be summarised here. The simple concept is to compare EBSPs acquired from pixels in the map to a nominally unstrained reference pattern of the same crystal orientation. An applied strain will change interplanar angles which moves Kikuchi bands in the diffraction pattern. Additionally, crystal orientation rotations will cause Kikuchi bands to move cooperatively across the screen. The diffraction pattern is segmented into 40 partially overlapping regions of interest (ROI), each of which undergoes a fast Fourier transform which is used for cross-correlation image analysis. From this, a translation vector for each region of interest is calculated relative to the corresponding ROI in the reference pattern. With four or more translation vectors, a self-consistent deformation tensor for the diffraction pattern can be built up with components for elastic strain and lattice rotations [39]. The anisotropic Hooke's law can be used to determine elastic stresses from strains with elastic constants from the Materials Project database [40,41]. Assuming surface traction free plane stress, the final ε_{33} strain component can be calculated [39].

The HR-EBSD analysis described above only accounts for elastic strain and stress. Plastic deformation by dislocations is more difficult to directly measure and calculate, but an indirect assessment based on deformation around dislocations can be conducted. As dislocations accumulate, they contribute to a net lattice curvature due to the extra half-planes of atoms. Lattice rotations are measured from the diffraction pattern by HR-EBSD as described above. The spatial gradient of the lattice rotations can be related to the density of geometrically necessary dislocations (GND) required to cause the measured lattice curvature [42]. The measured lattice curvature is a net effect of stored dislocations in the structure, not necessarily dislocations which have contributed to plastic deformation, and is a lower bound as dislocations of opposite sign will cancel out their effect on lattice curvature within a diffracting interaction volume [37]. Nye extended his derivation of curvature caused by a net density of dislocations into three dimensions as a tensor which can be solved based on lattice rotations and elastic strains measured using HR-EBSD [39,42]. With the angular and strain sensitivity of cross-correlation HR-EBSD, noise in GND density maps is $\sim 10^{12}$ m^{-2} [39].

Raman piezospectroscopic mapping was carried out on a Witec Alpha 300R confocal Raman microscope in the Materials Research Facility at UKAEA. A green 532 nm laser set to 10 mW was used to acquire spectra through a 100x objective lens with 0.5s integration time.

The confocal aperture was the 50 µm diameter optical fibre connecting the microscope to the spectrometer, which achieves depth resolution ~ 1 µm. The indent impression was scanned on a piezo-electric positioning stage to produce a map with step size of 200 nm. Spectra were acquired for each pixel in the map with curves fitted using a Lorentz function in Witec Project 5 software. The position of the SiC transverse optic peak (~789 cm^{-1}) was extracted to form maps of Raman peak position shift, $\Delta\omega$ relative to a nominally unstressed position in the same sample. An indented sample of single crystal silicon (001) was similarly investigated using the longitudinal optic peak at ~520 cm^{-1}.

Stress is linearly related to the change in Raman peak position by $\sigma = \Delta\omega \times R$ where R is a piezospectroscopic coefficient. This relationship depends on stress state where for hydrostatic stress, $\sigma = \frac{\Delta\omega \times R}{3}$, and for balanced biaxial stress $\sigma = \frac{\Delta\omega \times R}{2}$. For 6H-SiC, the coefficient of R=-849.9 MPa.cm from DiGregorio and Furtak is used [43]. This coefficient was calibrated using hydrostatic pressure but is considered by the authors to be a coefficient for average stress across all directions so could be applied to other stress states including biaxial. Raman stress mapping in silicon has been extensively studied, and the coefficients have been well characterised theoretically and experimentally [44–46]. The sign of the coefficient indicates that a shift to higher wavenumbers corresponds to a compressive residual stress, while a tensile stress state causes a shift to lower wavenumbers.

Table 1: Summary of Raman piezospectroscopic coefficients

Stress state	Coefficient, R (MPa.cm)	Ref.
Hydrostatic	-849.9 (6H-SiC TO peak ~789 cm^{-1})	[43]
Hydrostatic	-531.9±0.02 (Si LO peak ~520 cm^{-1})	[44]
Uniaxial	-434 (Si LO peak ~520 cm^{-1})	[45,46]
Biaxial	-434 (Si LO peak ~520 cm^{-1})	[45,46]

Results

The unirradiated indent impression shows radial surface cracks emanating from the corners of the indent impression (Figure 2 (a)). These radial surface cracks were 4.24 µm long, corresponding to an indentation fracture toughness of 2.71 MPa√m using the modified Laugier equation [7] with the fitting coefficient of 0.022 from Cuadrado *et al.* [9].

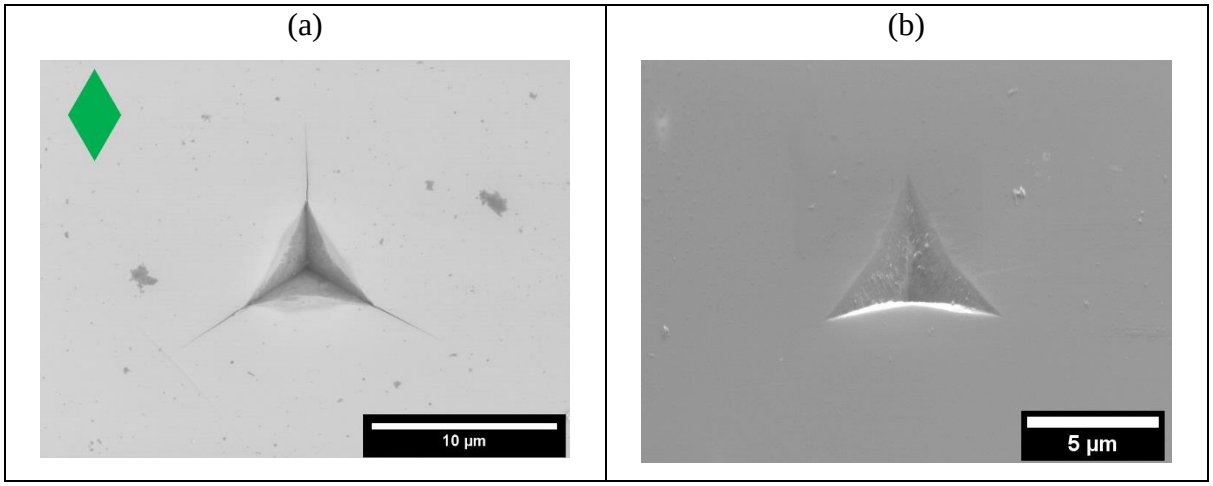

Figure 2: (a) SEM micrograph of a 1000 nm Berkovich indent in 6H-SiC with the crystallographic unit cell orientation shown. (b) 1000 nm Berkovich indent in irradiated 6H-SiC at the same crystallographic orientation as (a). No radial cracks.

HR-EBSD maps of the components of the plane stress tensor are shown in Figure 3. This displays the residual elastic deformation around the indent impression, showing large compressive stresses below the face of the indenter (σ_{22} component), and tensile stresses ahead of the crack tip reaching 600 MPa in the σ_{11} component.

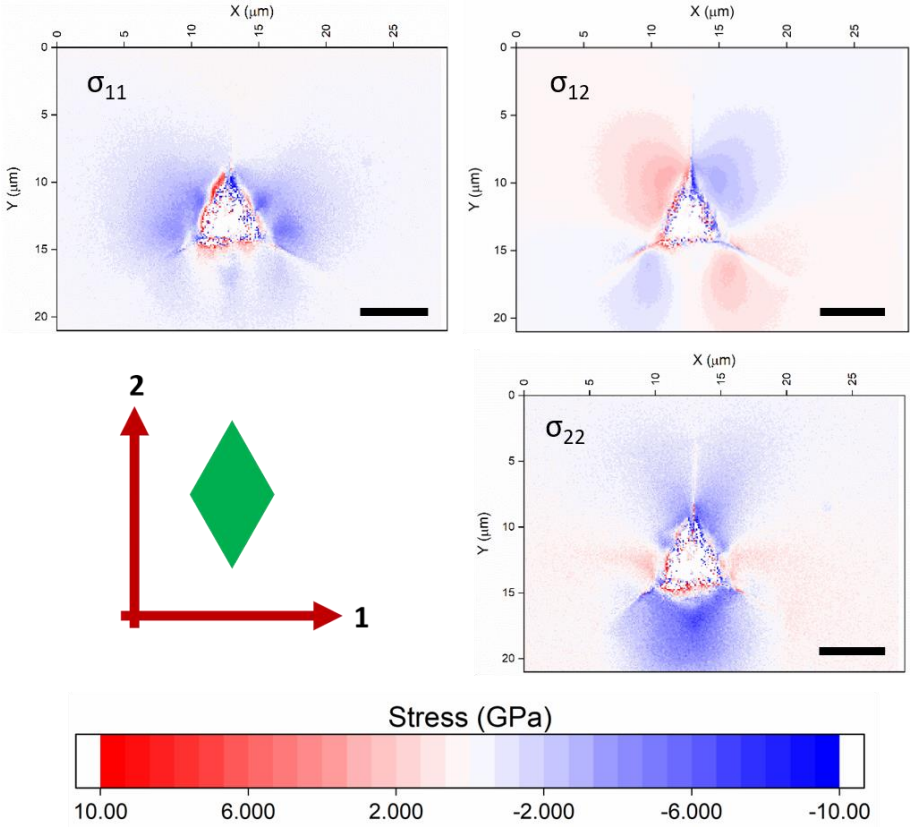

Figure 3: HR-EBSD plane stress tensor of a 1000 nm Berkovich indent in 6H-SiC. Scale bar is 5 µm. Axes and crystal unit cell orientation are shown in the lower left.

The total elastic deformation around this indent impression can more clearly be seen in the planar von Mises stress and biaxial stress maps in Figure 4. There is clear stress relief along

the cracks, and a lower residual elastic stress near the indent impression where there is a region of high GND density, shown in Figure 5. The presence of geometrically necessary dislocations (GNDs) can be indicative of residual plastic deformation. Without irradiation, residual plastic deformation is localised near the indent impression, approximately in the region of lower residual elastic deformation observed in the elastic stress maps in Figure 3 and Figure 4. Cracks can clearly be seen as discontinuities in lattice curvature. The area of high GND density is in an approximate circle connecting the corners of the indent impression.

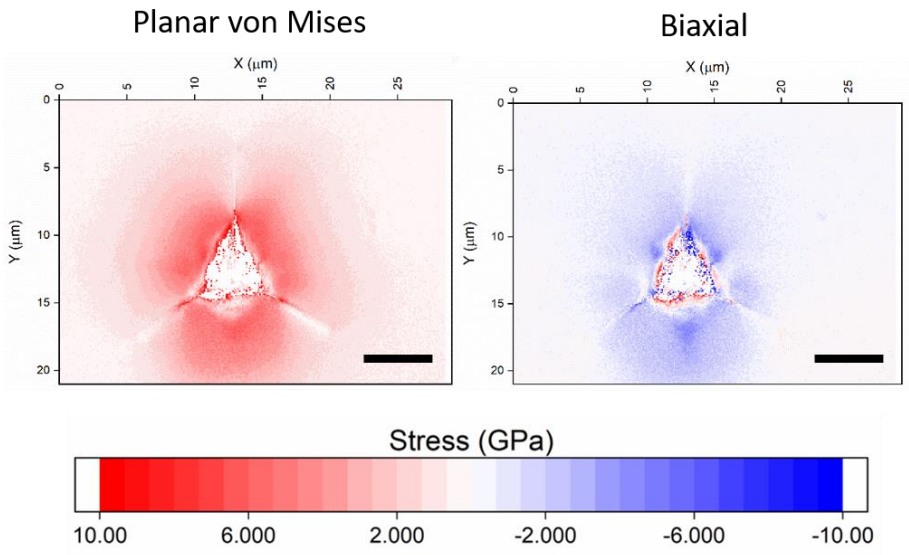

Figure 4: Planar von Mises and biaxial stress maps of a 1000 nm Berkovich indent in 6H-SiC. Scale bar is 5 µm.

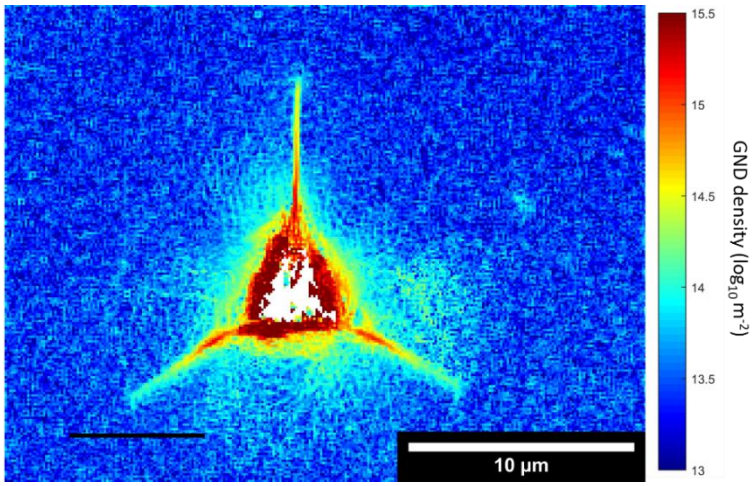

Figure 5: GND density map around a 1000 nm Berkovich indent in 6H-SiC.

Raman piezospectroscopic mapping (Figure 6) shows a qualitatively similar spatial variation of residual elastic stress as the HR-EBSD biaxial stress maps shown above. Stress relief is seen along the cracks, and a lower compressive elastic stress is seen close to the indent impression possibly caused by plastic deformation, pile-up, or sub-surface fracture which do not contribute to Raman peak shifts. Tensile stress is seen at the crack tips. The peak shift at

the crack tips is -1.3 cm^{-1} corresponding to a uniaxial tensile stress of 368 MPa. The maximum peak shift in the compressive regions is +1.8 cm^{-1}. Assuming a hydrostatic stress state, σ = -510 MPa. If DiGregorio and Furtak are correct in claiming their piezospectroscopic coefficient is valid in non-hydrostatic conditions, an assumed biaxial stress would be -765 MPa and a uniaxial (σ_{22}) stress of -1.53 GPa [43]. The stresses measured by Raman spectroscopy are considerably lower than measured by HR-EBSD. This is probably due to the larger interaction volume in this optically transparent single crystal incorporating some less strained material beneath the surface, despite the confocal aperture. Guo & Todd showed the effect of depth resolution on observed residual stress around indents in alumina [47]. Errors of greater than 40% could arise when non-confocal (~14 µm depth resolution) fluorescence mapping was used compared to confocal (~3 µm depth resolution in their experiments). The discrepancy in residual stress measured by HR-EBSD and Raman spectroscopy is related to the depth resolution (~40 nm in EBSD, ~1 µm in Raman), and the fact that residual stress around indents falls steeply below the specimen surface.

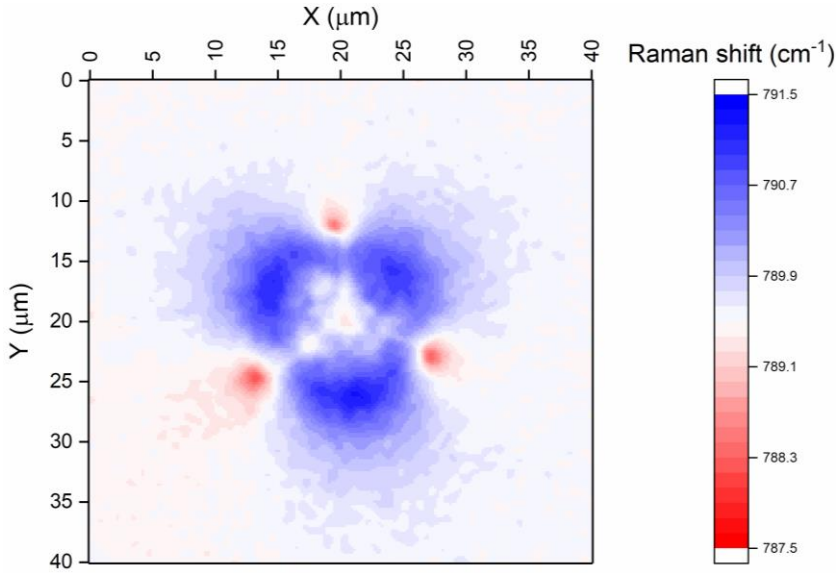

Figure 6: Raman piezospectroscopic map of a 1000 nm Berkovich indent in 6H-SiC. The colour scale is centred on 789.5 cm^{-1}, the position of the 6H-SiC TO peak away from the indent in nominally unstressed material.

FIB cross-sections of indents reveal sub-surface fracture. Videos of these experiments are provided in supplementary material. Figure 7 shows two sequential frames taken during FIB milling of an indent in unirradiated 6H-SiC. At a critical point, the radial surface cracks elongate by ~2.1 µm, indicating a change to the crack morphology. A bulge to the lower portion of the FIB cross-section face also appears at this point.

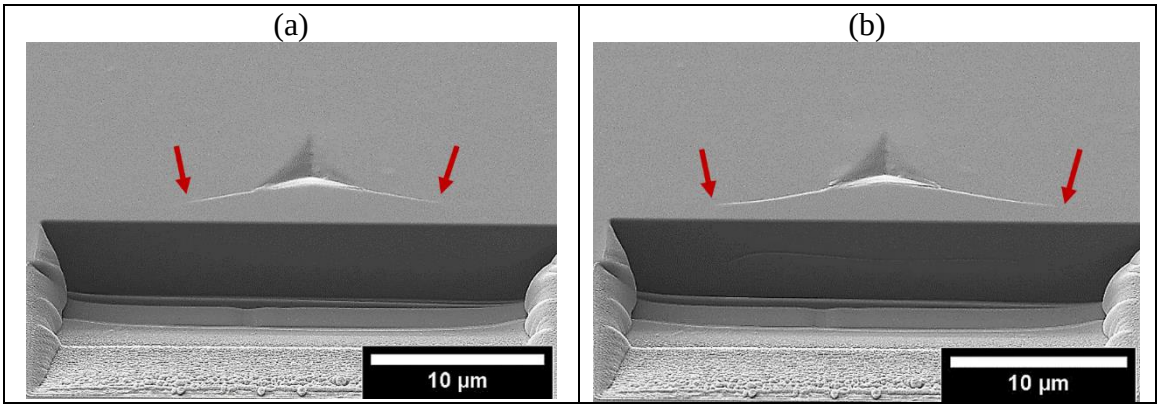

Figure 7: SEM images of FIB slicing of a 1000 nm Berkovich indent in 6H-SiC. Surface radial cracks in (a) are the same length as before milling. (b) shows the frame immediately after cracks have extended.

In the irradiated region of the same sample, indentation impressions showed no radial surface fracture (Figure 2 (b)). As the material remains crystalline, EBSD patterns were acquired to map the residual elastic deformation and calculate the residual GND density. Pattern quality was reduced due to radiation defects, which are discussed in **[reference Raman paper and nanoindentation paper**]. After irradiation, elastic deformation is localised near the indent (Figure 8 and Figure 9) , and reaches a higher relative magnitude of ~-6.5 GPa biaxial elastic stress. Residual shear stresses (σ_{12}) are higher after irradiation, as seen in the difference between the von Mises map, and the biaxial map.

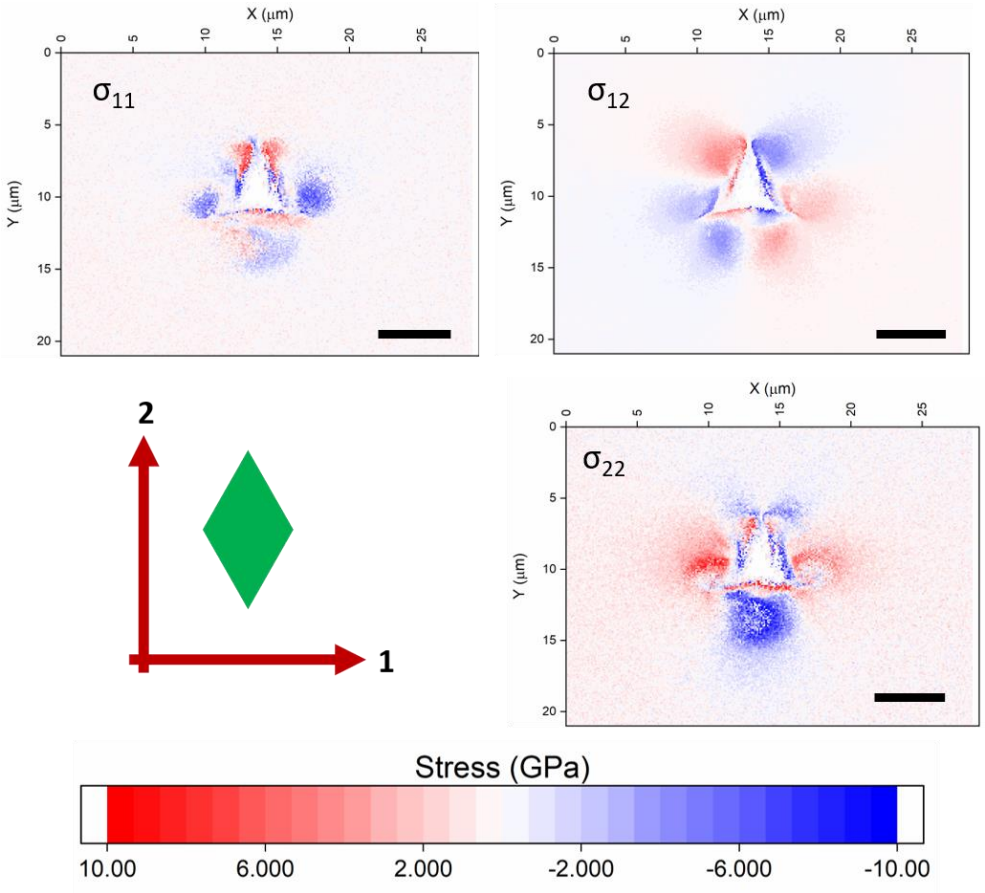

*Figure 8: HR-EBSD plane stress tensor of a 1000 nm Berkovich indent in irradiated 6H-SiC. Scale bar is 5 μm. Axes and crystal unit cell orientation are shown in the lower left. Stresses are relative to stress far from the indent, which is shown to be compressive [**reference nanoindentation/swelling paper]***

Elastic deformation is represented more clearly in plane stress von Mises and biaxial stress maps in Figure 9. Plastic deformation is represented by GND density in Figure 10. These maps again show no surface fracture. The GND density map shows plastic deformation extends further from the indent impression after irradiation, and reaches a higher dislocation density. The increase in background GND density is a physical effect of radiation damage and is discussed in **[reference indentation deformation paper]**.

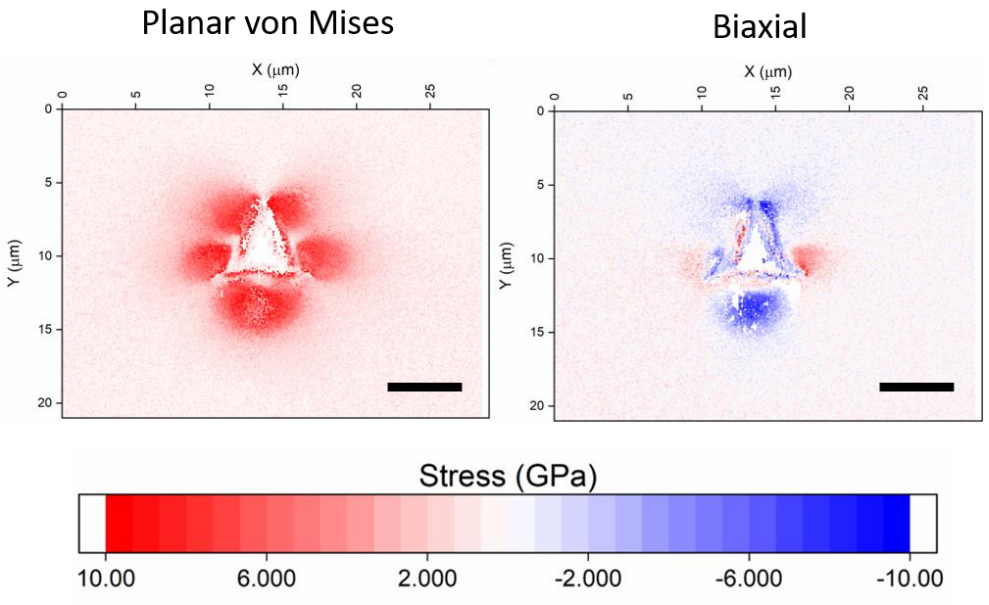

Figure 9: Planar von Mises and biaxial stress maps of a 1000 nm Berkovich indent in irradiated 6H-SiC. Scale bar is 5 µm.

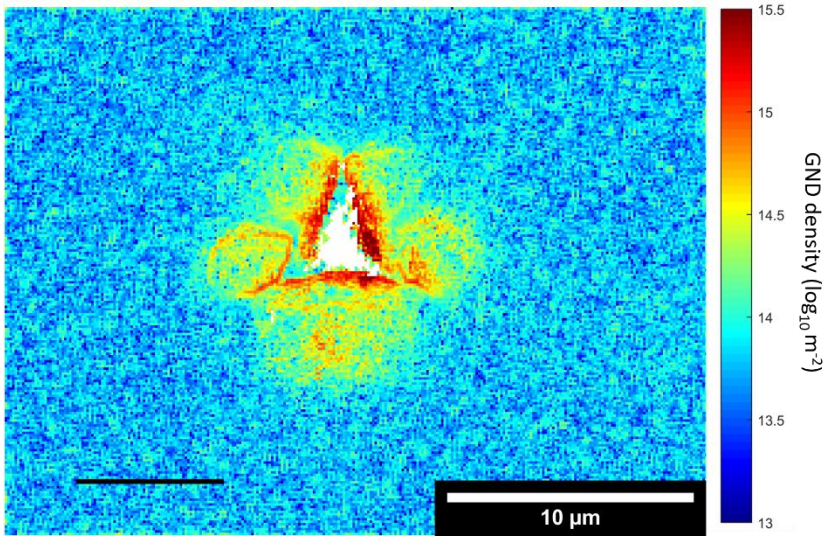

Figure 10: GND density map around a 1000 nm Berkovich indent in irradiated 6H-SiC.

Radiation defects in SiC preclude the mapping of residual stresses by piezo-Raman spectroscopy, however Raman spectra do provide information on radiation defects which we discuss in **[reference Raman paper].**

Cross-sectioning was again carried out on an indent in irradiated 6H-SiC (Figure 11). Before slicing there are no cracks. As material is removed, cracks grow stably from the lower corners of the indent impression (Figure 11 (a) to (b)). At a critical length, these cracks elongate in a similar manner to the unirradiated indent (Figure 11 (b) to (c)). With further slicing through the indent, two cracks appear from the upper indent corner (Figure 11 (d)). At the slice before cracks suddenly extend, the radial crack length is ~4 µm, similar to the unirradiated crack length before extension, and the extended crack length is also similar. The distance of the cross-

section away from the indent face is also similar. Of course, the stress state around the indent is very different, and the crack morphology is different, but the similarity in length is interesting.

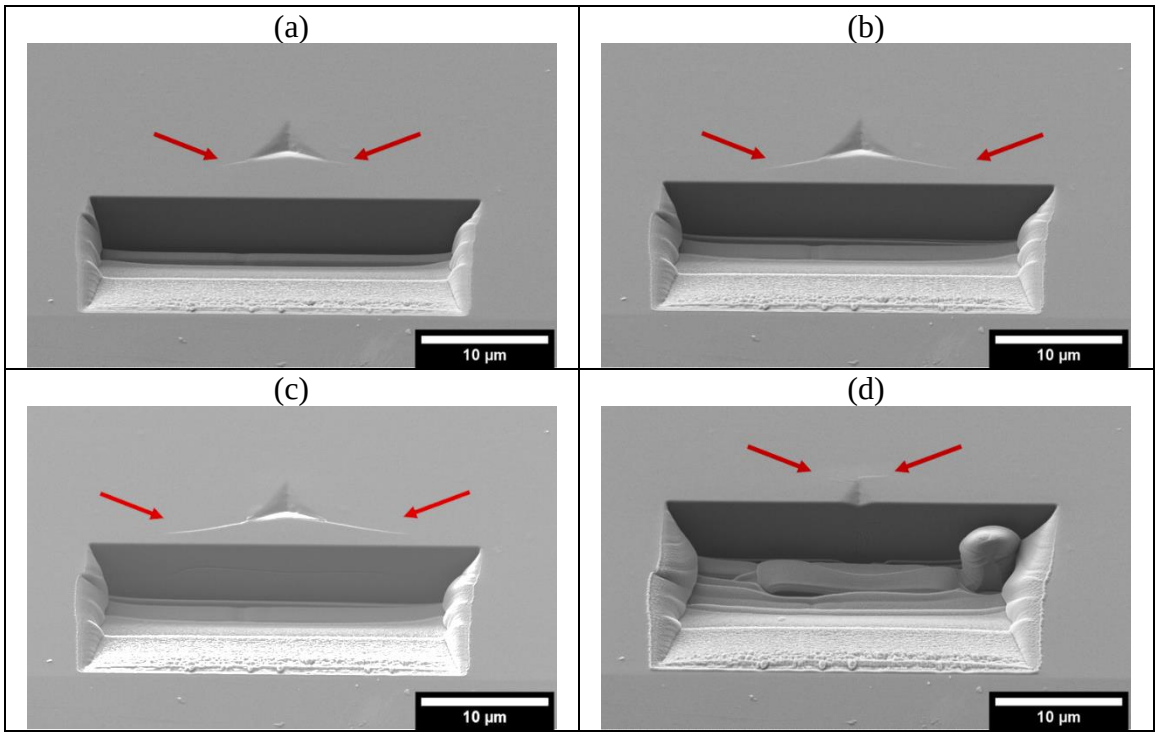

Figure 11: FIB slicing of an indent in irradiated 6H-SiC. (a) shows radial cracks growing from the lower corners of the indent impression as material is FIBed away. (b) is the slice immediately before cracks jump forward (c) is the slice immediately after. (d) shows two cracks growing from the top corner of the indent impression

To investigate the changes to stress state due to crack growth, FIB slicing was stopped immediately after the crack jumped. Unfortunately, the process of imaging using the FIB amorphises SiC preventing EBSD pattern collection and significantly altering Raman spectra so residual stress could not be measured directly in SiC after FIB slicing. Silicon shows similar features of crack extension during FIB slicing of indents, but its structure is more resistant to FIB damage than SiC, so Raman spectra could be collected for mapping after the experiment. Figure 12 shows the crack growth in silicon, and the Raman residual stress map. Typical features of tensile stress ahead of the crack tip and compressive stresses from the faces of the indent can be seen. The face of the indent where slicing was taking place and where cracks grew has had its compressive stress relieved, and no tensile stress is seen at the crack tips.

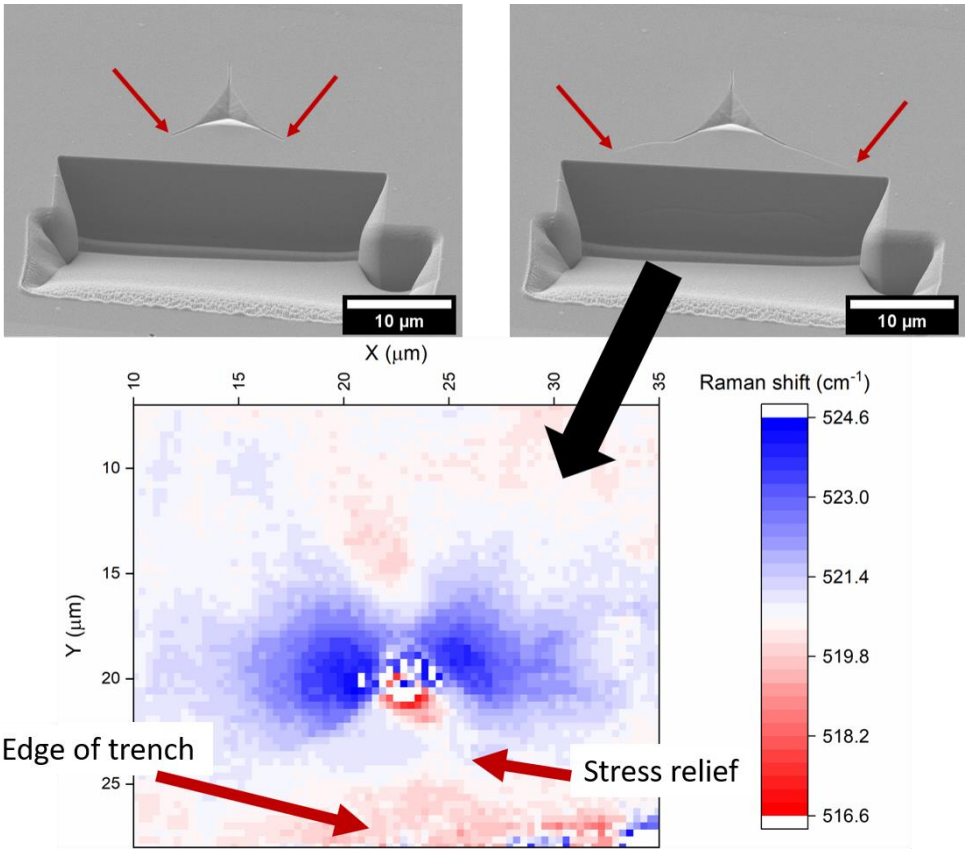

Figure 12: Crack growth during FIB cross-sectioning of a 1000 nm Berkovich indent in silicon (001) surface. Slicing was stopped immediately after crack growth and residual stress was mapped using Raman spectroscopy. The edge of the trench is indicated, along with the region of relieved stress.

The above experiments were conducted with FIB milling from an indent face towards the indent centre and opposite corner. This has relieved compressive stresses from the face allowing tensile hoop stress to grow the cracks, changing the crack morphology. To try to avoid this, a similar indent in unirradiated 6H-SiC was sliced from a corner towards the opposite face with a tapered milling shape to minimise material removal while still observing the radial corner crack. Figure 13 shows the radial crack which was initially 4.25 µm long has jumped forward to the edge of the milled trench 5.66 µm away.

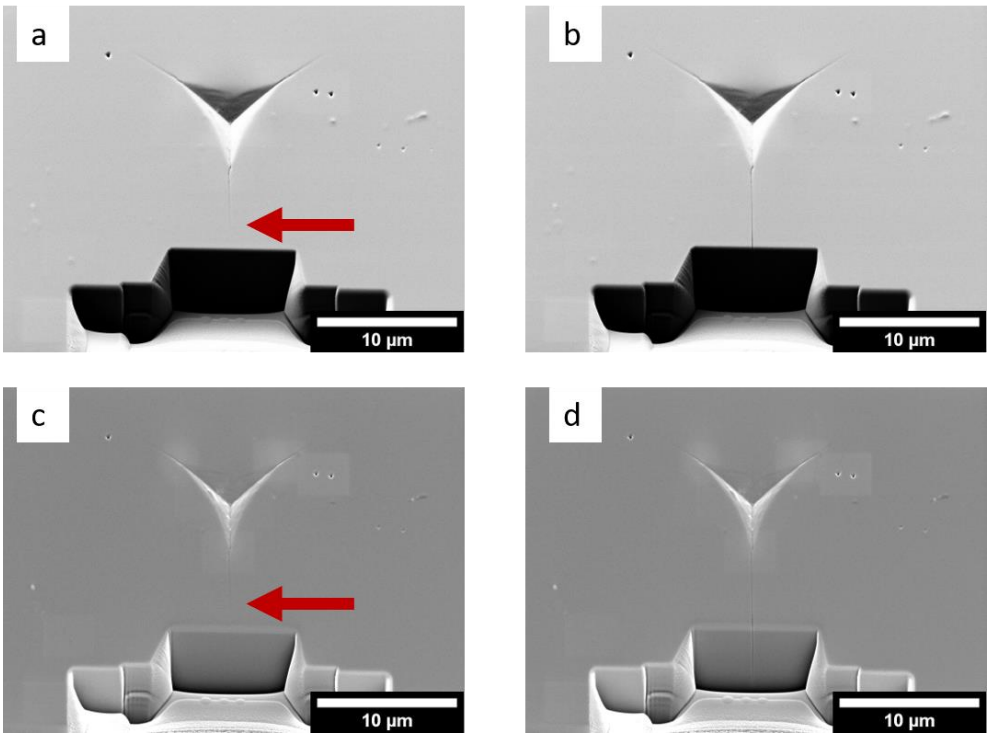

Figure 13: FIB slicing of unirradiated 6H-SiC from a corner. (a) and (b) use the SE detector, (c) and (d) use an in-lens detector which is oriented towards the cross-section face. Red arrows in (a) and (c) show the crack tip position, while (b) and (d) are the images immediately after crack growth where the crack has grown to the edge of the trench.

Further slicing though this indent shows a lateral crack branching from this radial crack connecting to the upper right radial crack (Figure 14). There is no left-hand crack at this point. The slight misalignment of the FIB trench may have favoured growth of this right-hand crack over the left-hand lateral crack.

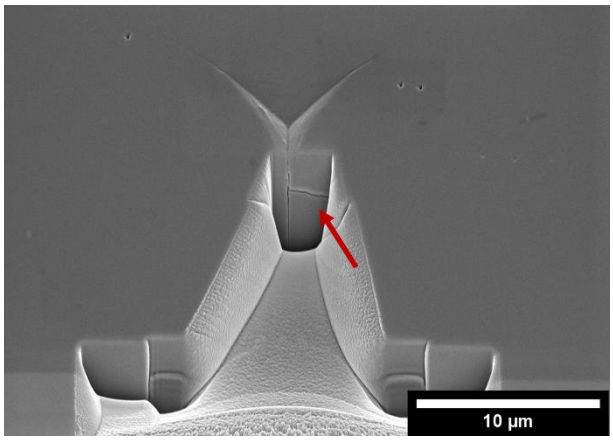

Figure 14: Lateral crack appearing during further slicing.

Slicing through the indent impression itself, the right-hand lateral crack initially is the only one. After a critical point, a left-hand lateral crack appears, coinciding with the upper left radial crack growing slightly (Figure 15). These cracks are appearing during FIB slicing – they are not there before slicing.

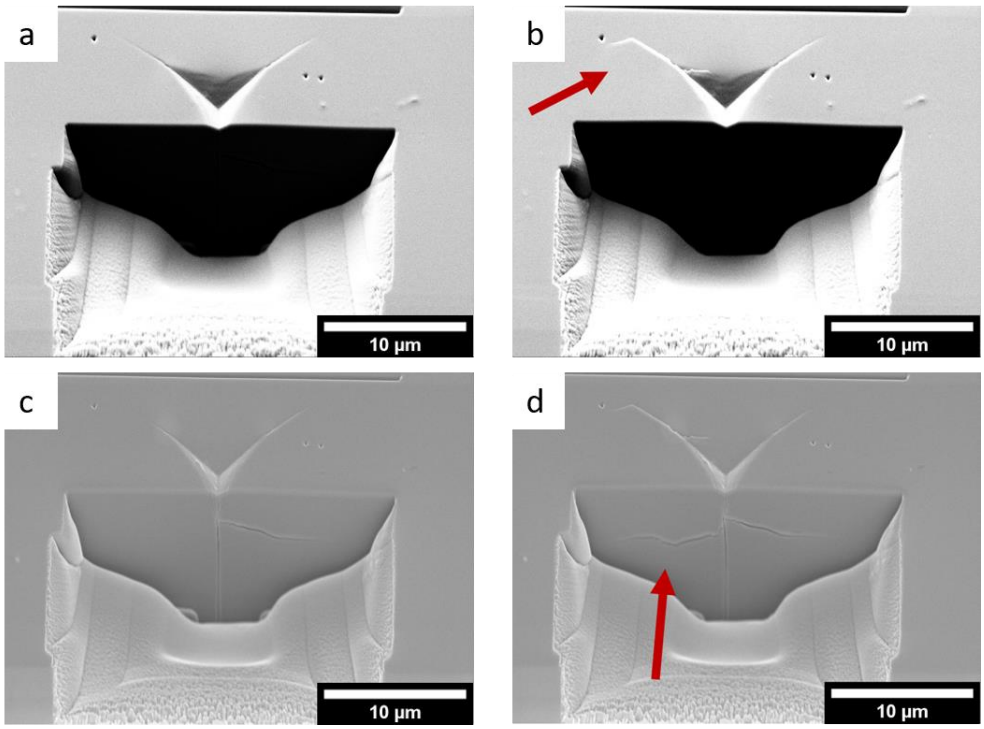

Figure 15: Corner milling through the indent impression of 6H-SiC. (a) and (b) are from the secondary electron detector. (c) and (d) from the in-lens detector. Initially only the right-hand crack which grew first can be seen. (b) and (d) show a left-hand lateral crack appearing, coinciding with the upper left radial crack growing, indicated with red arrows.

Discussion

6H-SiC fractures radially on the surface during nanoindentation – as one would expect. The residual stresses around the indent impression are significant and take the expected form; biaxial compressive stresses from the indent faces are large and counteract tensile hoop stresses at the crack tips, leaving crack growth in equilibrium. FIB slicing to reveal the sub-surface crack morphology removes constraining material from around the indent impression, leading to relief of the compressive stress in the direction of this new free surface. The now unopposed tensile hoop stress at the crack tips allows the radial cracks to grow.

The observation of radial cracks growing on the surface would suggest that sub-surface crack morphology is changing. It appears that under Berkovich nanoindents in silicon carbide, there are no lateral cracks until FIB cross-sectioning takes place, as shown in Figure 15. The process of revealing the sub-surface fracture morphology is *causing* sub-surface fracture. Depending on which direction FIB slicing takes place, residual stresses are relieved differently, thus cracks grow differently. This may explain the observation of different crack densities depending on which direction an indent was sliced [12,13].

Other researchers observed a bulging of the FIB slice face which they attributed to residual stresses around the indent impression [12,13]. Something similar is observed here,

most clearly in Figure 7 (b) and Figure 12. In these cases, the lower portion of the FIB slice face appears to be protruding further than the upper portion. The change in the FIB slice face coincides with crack growth. When the compressive stress is relieved by removing surrounding material, the compressed material expands outwards. This shields the lower part of the FIB slice face from the ion beam, thus it is left protruding as the beam moves further into the material.

The indent in irradiated 6H-SiC is particularly interesting and prompted further investigation of residual stresses in this material which is discussed in **[reference nanoindentation and residual stress paper].** The residual elastic and plastic deformation around this indent is significantly altered due to the presence of a compressive biaxial stress caused by the undamaged substrate of the specimen. It is also the reason surface radial cracking is prevented. The biaxial compressive stress is on the order of 6 GPa. FIB slicing relieves this radiation-induced compressive stress approximately linearly, allowing the stable crack growth seen in Figure 11 (a) – (b), and more clearly in the video online. At the end of this stable crack growth the crack length is approximately the same as in the unirradiated material – however the stress state is different so this may be a coincidence. The crack jumping from this point in FIB slicing is similar to what is seen in the unirradiated material. This may imply that the fracture properties of irradiated SiC are not significantly different to unirradiated SiC – the observed difference may only be due to biaxial residual stress from the substrate rather than fundamental differences in properties.

These results reinforce the evidence that the empirical equations for calculating fracture toughness of brittle materials using radial surface crack lengths and assumed sub-surface crack morphology are only useful for qualitative comparisons. This may fall apart if sub-surface fracture between two samples is different, and the assumption of crack morphology in the empirical equations is invalid. Destructive tomography, such as FIB slice and view, appears inappropriate for determining the sub-surface crack morphology for improving the empirical equations of fracture toughness. Residual stresses around indents are large and cause crack growth during FIB slicing. This is likely to be true for all brittle materials. Annealing samples may relieve residual stresses; however, this relief is likely to cause crack growth in a similar way to residual stress relief shown here, thus no improvement in observing sub-surface fracture caused by indentation.

FIB slice and view has been combined with HR-EBSD for 3D examination of deformation under nanoindents and within deformed micropillars in metals [48,49]. The observed stress release and evolution of deformation during FIB slicing in this work would

also be expected to alter the results of 3D HR-EBSD. The evolution of deformation during FIB slicing is probably less obvious in metals; indentation stress is typically accommodated by plasticity rather than fracture. Nevertheless, FIB slicing alters the stress state, thus what is observed and calculated by cross-section HR-EBSD is unlikely to be the stress state under the indent had the FIB slicing not been carried out. This may explain the differences in dislocation density calculated by destructive HR-EBSD and non-destructive XRD in reference [49]. Removing material and altering the stress state also extends to analysis using TEM or other lift-out or thin film techniques where constraints are removed. Convergent beam electron diffraction can make use of this effect to calculate residual stress in the original material based on stress relaxation during preparation of TEM lamellae [50]. What is observed in a lift-out specimen is different to what is in the bulk of a specimen.

Conclusions

It appears to be impossible to observe the true sub-surface fracture morphology of indents by FIB cross-sectioning due to the relief of residual stresses during milling. This is the case for any destructive technique where the stress state is altered. Altering residual stresses allows cracks to grow. This makes fracture toughness calculations based on crack morphology impossible to confirm, remaining reliant on assumptions.

The residual stresses and deformation around indents in unirradiated and ion irradiated 6H-SiC is considerably different due to biaxial compressive stresses in the sample. As the deformation mechanism is significantly altered, mechanical properties extracted from nanoindentation of ion implanted materials susceptible to swelling is likely to be incorrect. This includes, and is probably most apparent in measurements of fracture toughness where fracture is subdued.

Acknowledgements

Thanks to Dr Nianhua Peng at Surrey Ion Beam Centre for running the ion implantation, and to Chris Smith at the Materials Research Facility, UKAEA, for training on the Raman microscope. Raman spectroscopy was carried out at UKAEA's Materials Research Facility which has been funded by and is part of the UK's National Nuclear User Facility and Henry Royce Institute for Advanced Materials. The authors acknowledge use of characterisation facilities within the David Cockayne Centre for Electron Microscopy, Department of

Materials, University of Oxford, alongside financial support provided by the Henry Royce Institute (Grant ref EP/R010145/1). Financial support through the EPSRC Science and Technology of Fusion CDT [grant number EP/L01663X/1] is gratefully acknowledged. This work has been carried out within the framework of the EUROfusion Consortium and has received funding from the Euratom research and training programme 2014-2018 under grant agreement No 633053 and from the RCUK Energy Programme [grant number EP/T012250/1]. The views and opinions expressed here do not necessarily reflect those of the European Commission.

Reference

[1] B. Lawn, R. Wilshaw, Indentation fracture: principles and applications, J. Mater. Sci. 10 (1975) 1049–1081. doi:10.1007/BF00823224.

[2] G.R. ANSTIS, P. CHANTIKUL, B.R. LAWN, D.B. MARSHALL, A Critical Evaluation of Indentation Techniques for Measuring Fracture Toughness: I, Direct Crack Measurements, J. Am. Ceram. Soc. 64 (1981) 533–538. doi:10.1111/j.1151-2916.1981.tb10320.x.

[3] D.B. MARSHALL, B.R. LAWN, A.G. EVANS, Elastic/Plastic Indentation Damage in Ceramics: The Lateral Crack System, J. Am. Ceram. Soc. 65 (1982) 561–566. doi:10.1111/j.1151-2916.1982.tb10782.x.

[4] P. Hosemann, D. Kiener, Y. Wang, S.A. Maloy, Issues to consider using nano indentation on shallow ion beam irradiated materials, J. Nucl. Mater. 425 (2012) 136–139. doi:10.1016/j.jnucmat.2011.11.070.

[5] D.E.J. Armstrong, C.D. Hardie, J.S.K.L. Gibson, A.J. Bushby, P.D. Edmondson, S.G. Roberts, Small-scale characterisation of irradiated nuclear materials: Part II nanoindentation and micro-cantilever testing of ion irradiated nuclear materials, J. Nucl. Mater. 462 (2015) 374–381. doi:10.1016/j.jnucmat.2015.01.053.

[6] M.T. Laugier, Palmqvist indentation toughness in WC-Co composites, J. Mater. Sci. Lett. 6 (1987) 897–900. doi:10.1007/BF01729862.

[7] R.D. Dukino, M. V. Swain, Comparative Measurement of Indentation Fracture Toughness with Berkovich and Vickers Indenters, J. Am. Ceram. Soc. 75 (1992) 3299–3304. doi:10.1111/j.1151-2916.1992.tb04425.x.

[8] A. Datye, U. Schwarz, H.-T. Lin, Fracture Toughness Evaluation and Plastic Behavior

Law of a Single Crystal Silicon Carbide by Nanoindentation, Ceramics. 1 (2018) 198–210. doi:10.3390/ceramics1010017.

[9] N. Cuadrado, D. Casellas, M. Anglada, E. Jiménez-Piqué, Evaluation of fracture toughness of small volumes by means of cube-corner nanoindentation, Scr. Mater. 66 (2012) 670–673. doi:10.1016/j.scriptamat.2012.01.033.

[10] N. Bassim, K. Scott, L.A. Giannuzzi, Recent advances in focused ion beam technology and applications, MRS Bull. 39 (2014) 317–325. doi:10.1557/mrs.2014.52.

[11] L. Holzer, M. Cantoni, Review of FIB Tomography, in: I. Utke, S. Moshkalev, P. Russell (Eds.), Nanofabrication Using Focus. Ion Electron Beams Princ. Appl., Oxford University Press, Oxford, 2012: pp. 410–435. https://www.researchgate.net/profile/Lorenz_Holzer/publication/230996181_Review_of_FIB-tomography/links/0912f5069bd7683f33000000.pdf.

[12] B.J. Inkson, D. Leclere, F. Elfallagh, B. Derby, The effect of focused ion beam machining on residual stress and crack morphologies in alumina, J. Phys. Conf. Ser. 26 (2006) 219–222. doi:10.1088/1742-6596/26/1/052.

[13] F. Elfallagh, B.J. Inkson, 3D analysis of crack morphologies in silicate glass using FIB tomography, J. Eur. Ceram. Soc. 29 (2009) 47–52. doi:10.1016/j.jeurceramsoc.2008.05.042.

[14] N. Payraudeau, D. McGrouther, K.U. O'Kelly, Quantification of subsurface damage in a brittle insulating ceramic by three-dimensional focused ion beam tomography, Microsc. Microanal. 17 (2011) 240–245. doi:10.1017/S1431927610094523.

[15] A. Baggott, M. Mazaheri, B.J. Inkson, 3D characterisation of indentation induced sub-surface cracking in silicon nitride using FIB tomography, J. Eur. Ceram. Soc. 39 (2019) 3620–3626. doi:10.1016/j.jeurceramsoc.2019.05.012.

[16] G. Newsome, L.L. Snead, T. Hinoki, Y. Katoh, D. Peters, Evaluation of neutron irradiated silicon carbide and silicon carbide composites, J. Nucl. Mater. 371 (2007) 76–89. doi:10.1016/j.jnucmat.2007.05.007.

[17] Y. Katoh, L.L. Snead, C.H. Henager, A. Hasegawa, A. Kohyama, B. Riccardi, H. Hegeman, Current status and critical issues for development of SiC composites for fusion applications, J. Nucl. Mater. 367–370 (2007) 659–671. doi:10.1016/j.jnucmat.2007.03.032.

[18] C.F. Zhe, Silicon Carbide: Materials, Processing & Devices, CRC Press, 2003.

[19] Y. Katoh, L.L. Snead, C.H. Henager, T. Nozawa, T. Hinoki, a. Iveković, S. Novak, S.M. Gonzalez de Vicente, Current status and recent research achievements in SiC/SiC

composites, J. Nucl. Mater. 455 (2014) 387–397. doi:10.1016/j.jnucmat.2014.06.003.

[20] M.E. Sawan, L. Snead, S. Zinkle, Radiation damage parameters for SiC/SiC composite structure in fusion nuclear environment, Fusion Sci. Technol. 44 (2003) 150–154. doi:10.13182/FST03-A325.

[21] T. Koyanagi, Y. Katoh, T. Nozawa, L.L. Snead, S. Kondo, C.H. Henager, M. Ferraris, T. Hinoki, Q. Huang, Recent progress in the development of SiC composites for nuclear fusion applications, J. Nucl. Mater. 511 (2018) 544–555. doi:10.1016/j.jnucmat.2018.06.017.

[22] A. Iveković, S. Novak, G. Dražić, D. Blagoeva, S.G. de Vicente, Current status and prospects of SiCf/SiC for fusion structural applications, J. Eur. Ceram. Soc. 33 (2013) 1577–1589. doi:10.1016/j.jeurceramsoc.2013.02.013.

[23] T. Hinoki, Y. Katoh, L.L. Snead, H.-C. Jung, K. Ozawa, H. Katsui, Z.-H. Zhong, S. Kondo, Y.-H. Park, C. Shih, C.M. Parish, R.A. Meisner, A. Hasegawa, Silicon Carbide and Silicon Carbide Composites for Fusion Reactor Application, Mater. Trans. 54 (2013) 472–476. doi:10.2320/matertrans.MG201206.

[24] R.. Jones, L. Giancarli, A. Hasegawa, Y. Katoh, A. Kohyama, B. Riccardi, L.. Snead, W.. Weber, Promise and challenges of SiCf/SiC composites for fusion energy applications, J. Nucl. Mater. 307–311 (2002) 1057–1072. doi:10.1016/S0022-3115(02)00976-5.

[25] S.J. Zinkle, L.L. Snead, Opportunities and limitations for ion beams in radiation effects studies: Bridging critical gaps between charged particle and neutron irradiations, Scr. Mater. 143 (2018) 154–160. doi:10.1016/j.scriptamat.2017.06.041.

[26] G.S. Was, Challenges to the use of ion irradiation for emulating reactor irradiation, J. Mater. Res. 30 (2015) 1158–1182. doi:10.1557/jmr.2015.73.

[27] C. Jiang, L. Dagault, V. Audurier, C. Tromas, A. Declémy, M.F. Beaufort, J.F. Barbot, Strain buildup in 4H-SiC implanted with noble gases at low dose, Mater. Today Proc. 5 (2018) 14722–14731. doi:10.1016/j.matpr.2018.03.062.

[28] S. Nogami, A. Hasegawa, L.L. Snead, Indentation fracture toughness of neutron irradiated silicon carbide, J. Nucl. Mater. 307–311 (2002) 1163–1167. doi:10.1016/S0022-3115(02)01055-3.

[29] X. Chen, W. Zhou, Q. Feng, J. Zheng, X. Liu, B. Tang, J. Li, J. Xue, S. Peng, Irradiation effects in 6H–SiC induced by neutron and heavy ions: Raman spectroscopy and high-resolution XRD analysis, J. Nucl. Mater. 478 (2016) 215–221. doi:10.1016/j.jnucmat.2016.06.020.

[30] A.J. Leide, L.W. Hobbs, Z. Wang, D. Chen, L. Shao, J. Li, The role of chemical disorder and structural freedom in radiation-induced amorphization of silicon carbide deduced from electron spectroscopy and ab initio simulations, J. Nucl. Mater. 514 (2019) 299–310. doi:10.1016/j.jnucmat.2018.11.036.

[31] J.F. Ziegler, M.D. Ziegler, J.P. Biersack, SRIM - The stopping and range of ions in matter (2010), Nucl. Instruments Methods Phys. Res. Sect. B Beam Interact. with Mater. Atoms. 268 (2010) 1818–1823. doi:10.1016/j.nimb.2010.02.091.

[32] R.E. Stoller, M.B. Toloczko, G.S. Was, A.G. Certain, S. Dwaraknath, F.A. Garner, On the use of SRIM for computing radiation damage exposure, Nucl. Instruments Methods Phys. Res. Sect. B Beam Interact. with Mater. Atoms. 310 (2013) 75–80. doi:10.1016/j.nimb.2013.05.008.

[33] R. Devanathan, W.J. Weber, Displacement energy surface in 3C and 6H SiC, J. Nucl. Mater. 278 (2000) 258–265. doi:10.1016/S0022-3115(99)00266-4.

[34] T.B. Britton, I. Holton, G. Meaden, D. Dingley, High angular resolution electron backscatter diffraction : measurement of strain in functional and structural materials, (2013) 8–13.

[35] T.B. Britton, A.J. Wilkinson, Measurement of residual elastic strain and lattice rotations with high resolution electron backscatter diffraction, Ultramicroscopy. 111 (2011) 1395–1404. doi:10.1016/j.ultramic.2011.05.007.

[36] T.B. Britton, A.J. Wilkinson, High resolution electron backscatter diffraction measurements of elastic strain variations in the presence of larger lattice rotations, Ultramicroscopy. 114 (2012) 82–95. doi:10.1016/j.ultramic.2012.01.004.

[37] T. Ben Britton, J. Jiang, P.S. Karamched, A.J. Wilkinson, Probing Deformation and Revealing Microstructural Mechanisms with Cross-Correlation-Based, High-Resolution Electron Backscatter Diffraction, JOM. 65 (2013) 1245–1253. doi:10.1007/s11837-013-0680-6.

[38] T.B. Britton, J.L.R. Hickey, Understanding deformation with high angular resolution electron backscatter diffraction (HR-EBSD), IOP Conf. Ser. Mater. Sci. Eng. 304 (2018) 012003. doi:10.1088/1757-899X/304/1/012003.

[39] A.J. Wilkinson, D. Randman, Determination of elastic strain fields and geometrically necessary dislocation distributions near nanoindents using electron back scatter diffraction, Philos. Mag. 90 (2010) 1159–1177. doi:10.1080/14786430903304145.

[40] K. Persson, Materials Data on SiC (SG:186) by Materials Project, (2014). doi:10.17188/1293198.

[41] M. De Jong, W. Chen, T. Angsten, A. Jain, R. Notestine, A. Gamst, M. Sluiter, C. Krishna Ande, S. Van Der Zwaag, J.J. Plata, C. Toher, S. Curtarolo, G. Ceder, K.A. Persson, M. Asta, C.K. Ande, S. Van Der Zwaag, J.J. Plata, C. Toher, S. Curtarolo, G. Ceder, K.A. Persson, M. Asta, Charting the complete elastic properties of inorganic crystalline compounds, Sci. Data. 2 (2015) 1–13. doi:10.1038/sdata.2015.9.

[42] J.. Nye, Some geometrical relations in dislocated crystals, Acta Metall. 1 (1953) 153–162. doi:10.1016/0001-6160(53)90054-6.

[43] J.F. DiGregorio, T.E. Furtak, Analysis of Residual Stress in 6H-SiC Particles within Al2O3/SiC Composites through Raman Spectroscopy, J. Am. Ceram. Soc. 75 (1992) 1854–1857. doi:10.1111/j.1151-2916.1992.tb07207.x.

[44] E. Anastassakis, A. Cantarero, M. Cardona, Piezo-Raman measurements and anharmonic parameters in silicon and diamond, Phys. Rev. B. 41 (1990) 7529–7535. doi:10.1103/PhysRevB.41.7529.

[45] I. De Wolf, Micro-Raman spectroscopy to study local mechanical stress in silicon integrated circuits, Semicond. Sci. Technol. 11 (1996) 139–154. doi:10.1088/0268-1242/11/2/001.

[46] Y. Kang, Y. Qiu, Z. Lei, M. Hu, An application of Raman spectroscopy on the measurement of residual stress in porous silicon, Opt. Lasers Eng. 43 (2005) 847–855. doi:10.1016/j.optlaseng.2004.09.005.

[47] S. Guo, A. Limpichaipanit, R.I. Todd, High resolution optical microprobe investigation of surface grinding stresses in Al2O3 and Al2O3/SiC nanocomposites, J. Eur. Ceram. Soc. 31 (2011) 97–109. doi:10.1016/j.jeurceramsoc.2010.08.021.

[48] N. Zaafarani, D. Raabe, R.N. Singh, F. Roters, S. Zaefferer, Three-dimensional investigation of the texture and microstructure below a nanoindent in a Cu single crystal using 3D EBSD and crystal plasticity finite element simulations, Acta Mater. 54 (2006) 1863–1876. doi:10.1016/j.actamat.2005.12.014.

[49] S. Kalácska, Z. Dankházi, G. Zilahi, X. Maeder, J. Michler, D. Ispánovity, I. Groma, Investigation of geometrically necessary dislocation structures in compressed Cu micropillars by 3-dimensional HR-EBSD, (2019). https://arxiv.org/pdf/1906.06980.pdf.

[50] L. Clément, R. Pantel, L.F.T. Kwakman, J.L. Rouvière, Strain measurements by convergent-beam electron diffraction: The importance of stress relaxation in lamella preparations, Appl. Phys. Lett. 85 (2004) 651–653. doi:10.1063/1.1774275.